Dedicated to my Parents, Family and Supervisor

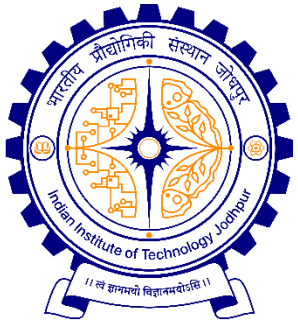


Certificate

I hereby declare that the work presented in this thesis, titled "**Management of Mitochondrial Oxidative Stress and Neurogenesis using Bioengineered Nanomedicine Platform**" submitted by **Shubham Garg,** to the Department of Bioscience and Bioengineering, Indian Institute of Technology, Jodhpur, Rajasthan, India in partial fulfilment of the requirements for the degree of Doctor of Philosophy, is a genuine record of the research carried out under my supervision and guidance. I confirm that the contents of this thesis, in whole or in part, have not been submitted to any other institute or university, either in India or abroad, for the award of any degree or diploma.

Date

Signature
Prof. Surajit Ghosh
Department of Bioscience and Bioengineering
Indian Institute of Technology, Jodhpur
Rajasthan, India 342037



Declaration

I hereby declare that the research work entitled "**Management of Mitochondrial Oxidative Stress and Neurogenesis using Bioengineered Nanomedicine Platform"** is original work conducted by me, carried out under the valuable supervision of **Prof. Surajit Ghosh,** Professor, Department of Bioscience and Bioengineering, Indian Institute of Technology Jodhpur, Rajasthan, India.

I confirm that the content of this thesis is original and has not been submitted, either in full or in part, to any university or institution for the award of any academic degree, diploma, certificate, associateship, fellowship, or any equivalent qualification. Contributions from other researchers, authors, or collaborators referenced in this work have been appropriately credited.



Signature
Date

Name: **Shubham Garg**
Roll No: **P19BB013**

Acknowledgement

As I stand on the precipice of concluding my Ph.D., I am imbued with a deep sense of accomplishment and eager anticipation for the future. The countless hours of research and hard work have all led to this moment of nearing the completion of my academic journey. Completing this thesis has been not only an academic challenge but also a profound journey of personal and philosophical growth. **I would like to express my deepest gratitude to my supervisor, Professor Surajit Ghosh, for his constant support and valuable feedback throughout my research journey. His commitment to academic excellence and attention to detail have been crucial in shaping this thesis. I am truly thankful for his guidance and mentorship, which have helped me overcome the challenges I faced during the completion of my PhD journey. Professor Ghosh's expertise and dedication have pushed me to achieve new levels in my academic work. His encouragement and belief in my abilities have motivated me to strive for excellence in every aspect of my research. His mentorship has not only improved my skills but also given me the confidence and determination to succeed as a scholar.** I am equally thankful to the members of my thesis committee, Prof. Indranil Banerjee, Prof. Shankar Manoharan, and Prof. Ananya Debnath, for their constructive feedback and essential suggestions that enhanced the quality of my work. Their expertise and guidance were invaluable throughout the research process, and I am grateful for their support in helping me achieve my academic goals. I am deeply grateful to the esteemed professors, staff, and fellow researchers from the Departments of Bioscience and Bioengineering, as well as Chemistry, at IIT Jodhpur, whose unwavering support has been instrumental in my academic journey. Each of them has played a pivotal role in helping me navigate the complexities of my research. My heartfelt appreciation extends to the entire CRDSI team at IIT Jodhpur, especially Dr. Jayita Sarkar, the Senior Scientific Officer, and the dedicated technical staff, Mukesh Sir, Pavan Sir and Sanjay Ji. Their tireless assistance and patience were crucial to carrying out the experimental analyses that formed the backbone of this thesis. In addition, I would also like to extend my sincere thanks to Prof. Prashunpriya Nayak of AIIMS Jodhpur, Prof. Heera Ram from Jai Narayan Vyas University (JNVU), and Prof. Amitva Das from IISER Kolkata, whose tremendous support with animal studies and electron microscopy imaging has been indispensable.

Something I learned multiple times throughout my time working on the Ph.D. is that graduate school is a marathon, not a race. There were many times when I felt like I was sprinting, fueled by the death of my stem cells or going several days without getting any blot in Western (the technique biologist loves to hate). Many other times, I felt exhausted and out of breath, wondering if I really could reach the finish line. Well, I have completed this marathon, and it would not have been possible without having a supportive group of people who have trained me, cheered for me, or provided homemade (read: hostel) food breaks along the way. Fortunately for me, I have had a lot of people cheering me on. Perhaps not so fortunate for you, that means reading these acknowledgements is a marathon of its own.

I would like to convey my heartfelt gratitude to my parents, whose unwavering support has been my anchor throughout this journey. I would also like to sincerely thank my elder sister, Ronak Garg, and my brother-in-law, Mayank Somya, for always looking after the family and allowing me to focus on my Ph.D. without any distractions. Their selflessness and dedication to ensuring everything ran smoothly at home provided me with the peace of mind needed to immerse myself fully in my academic work. Not only did they provide me with emotional strength, but they also stepped in with crucial financial assistance when unexpected personal

challenges arose. Without their selfless contributions, I would not have been able to navigate the hurdles I faced.

Throughout my Ph.D., I have learned the most not only in terms of science but also in friendship and camaraderie from my fellow group mates, seniors and Juniors. I am deeply thankful to the seniors I've had the pleasure of working with: Dr. Moumita Jash, Dr. Samya Sen, Dr. Varsha Gupta, Dr. Juhee Khan, Dr. Prabir K. Gharai, Dr. Rathnam Mallesh. I am thankful to Dr. Varsha Gupta and Dr. Juhee Khan for being with me throughout my initial days of learning in the lab. A special thanks goes to Dr. Juhee Khan for getting me started with animal work and always encouraging me along the way in professional development. Even more than that, I am thankful for the confidence she has given me in performing animal surgeries. I'm grateful to Dr. Prabir K. Gharai, Dr. Rathnam Mallesh for being my dinner buddy and a constant source of help and advice. During my time at IIT Jodhpur, I have also seized opportunities to learn from my excellent colleagues turned friends. I express my love and regards to them: Nabanita, Satyajit, Ramkamal, Surojit, Sanju, Rajsekhar, Aniket, Umar, Shubhadra, Debasmita, Monica, Adel, Dipro, Moumit for their constant support. I'm also grateful to Mr. Vijendra Singh Tomar Ji for expediting the delivery of chemicals.

Last but certainly not least, I wish to express my heartfelt gratitude to my friends (my certainty in uncertainty) Vijaylaxmi, Jay, Lavanya, Kushal, Parvathy, Shivangi, Som, Yuvraj Arti, Rahul, Akshay, Ashish, Siddharth, Apoorva, Simangka, Ashita and Shashank who provided both distractions when needed and encouragement when it seemed impossible to continue. Their unwavering support has been like a constantly descending gradient on the path towards achieving global optima, gently pushing me forward, helping me navigate past obstacles, and encouraging me to leap beyond the confines of local optima. Their belief in me has been a constant source of motivation, and I am truly thankful for their love, patience, and encouragement throughout this journey.

Shubham Garg
Department of Bioscience and Bioengineering
Indian Institute of Technology, Jodhpur
Rajasthan, India 342037

Abstract

This thesis entitled "Management of Mitochondrial Oxidative Stress and Neurogenesis using Bioengineered Nanomedicine Platform" talks about the development of various therapeutics for the treatment of oxidative stress in the central nervous system (CNS) and peripheral nervous system (PNS). The complex pathophysiology of traumatic brain injury (TBI) is a major obstacle, as it includes the central nervous system's (CNS) limited regenerative capacity and an overabundance of reactive oxygen species (ROS). Another challenge is the blood-brain barrier (BBB), which limits the ability to distribute therapeutic medicines to areas that are inflammatory. To address these difficulties, we developed a new approach to treatment using polydopamine (PDA)-coated mesoporous silicon nanoparticles (PDA-AMSNs) to transport a neurochemical modulator (NCM), a possible inhibitor of glycogen synthase kinase-3β (GSK-3β). A multifunctional therapeutic matrix was created by integrating these nanoparticles with a PANAP hydrogel, which is known for its neuroprotective properties. We created a logic AND gate circuit with PDA-AMSNs and NCM as inputs and neuroprotection as output by injecting this composite system, PDA-AMSN-D, into a cryogenic brain injury (CBI) model. The results highlighted the system's potential for TBI management by demonstrating significant therapeutic efficacy, which included a reduction in infarct volume, enhancement of neurogenesis, restoration of BBB integrity, and improved neurological recovery.

This thesis also talks about the design and development of novel mitochondria targeting gallic acid-derived small-molecule drugs for the alleviation of oxidative stress in LPS-induced neuroinflammation. The Overproduction of reactive oxygen species (ROS) by mitochondria, which are essential for cellular homeostasis and energetics, can cause oxidative stress. Neuroinflammation and neurodegeneration are significantly associated with mitochondrial dysfunction. In response to these concerns, we created Mito-TBA, an antioxidant that targets mitochondria and is based on gallic acid and the mitochondriotropic triphenylphosphonium (TPP) cation. Significant anti-inflammatory and antioxidative effects were shown by this new chemical, Mito-TBA-3. In vitro studies demonstrated that Mito-TBA-3 protects neurones derived from PC-12 by inhibiting mitoautophagy, attenuating the activation of lipopolysaccharide-induced toll-like receptor 4 (TLR-4), and activating the Nrf-2/ARE pathway. In a rat model of neuroinflammation caused by LPS, Mito-TBA-3 restored memory loss, reduced depressive symptoms, prevented further inflammation, and lowered levels of proinflammatory cytokines. One possible treatment possibility for neurodegenerative illnesses related to mitochondrial oxidative stress is this chemical, which outperformed aspirin, a commonly used NSAID. Debilitating neuropathies and functional deficits can result from peripheral nerve injuries, especially those that impact the sciatic nerve.

Further, this thesis talks about the development of novel peptide-derived scaffolds for nerve regeneration on PNS. For nerve restoration to be successful, it is necessary to precisely align the fascicles so that the nerve sprouts and Büngner bands can reattach. Although autogenous nerve grafting is still highly recommended, it does have certain drawbacks, such as donor site morbidity and inadequate repair efficacy. There is a lack of therapeutic potential in current tissue-engineered nerve scaffolds due to their absence of electrical conductivity, fibre alignment, and components of the extracellular matrix (ECM). A nanofibrous ECM-mimicking self-assembling peptide hydrogel, including neuroregenerative motifs (NAP and NAV) and a self-assembling motif ($K_2(SL)_6K_2$) was devised to address these challenges. Important for directing stem cell orientation and encouraging neurite outgrowth, this

hydrogel displayed topographical patterns on a nanoscale. Using morphological and histological investigations, functional assessments, and gastrocnemius muscle reinnervation, the hydrogel enabled structural healing and functional recovery within two weeks in a rat model of sciatic nerve injury. These results demonstrate that hydrogel may be a viable therapeutic option for repairing peripheral nerves.

Overall, this thesis gives a glimpse where combining these three treatment modalities highlights the need for new ways to deal with central nervous system trauma, neuroinflammation, and peripheral nerve injury. Each approach takes advantage of ideas from bioinspired design to provide specific, efficient therapies for nerve and neurological disorders. They open the door to a new age of precision medicine and give patients with diseases that were thought to be incurable a glimmer of hope.

PhD Course Work: Completed

Number of credits opted: 35

Status: Completed 35 credits in December 2020 with a CGPA: 8.16

Publications:

1. Garg, S.,[#] Jana, A.,[#] Gupta, S., Arshi, M.U., Gharai, P., Khan, J., Roy, R., and Ghosh, S., **2024**. Discovery of Gallic Acid Based Mitochondriotropic Antioxidant Attenuates LPS Induced Neuroinflammation. *Free Radic. Biol. Med. 226, pp. 302-329*

2. Jana, A.,[#] **Garg, S.,**[#] Ghosh,S., Khan, J., Roy, R., Mukherjee, N., Jash, M., Gupta, V., Nayak, P. and Ghosh, S., **2024**. Generation of Functional Neurons from Mesenchymal Stem Cells Using Neural Differentiator and Engineered Peptide Hydrogel: Potential Therapeutic Lead for Traumatic Brain Injury. *ACS Appl. Mater. Interfaces., 16, 47, 64476-64493*

3. Khan, J., Gharai, P.K., **Garg, S.,** Gupta, S., Arshi, M.U., Mallesh, R. and Ghosh, S., **2024**. Discovery of Powerful Multifaceted Antioxidant for Combating Oxidative Stress Associated with Neurodegenerative Disorders. *Acta Pharm. Sin. B., (Just Accepted)*

4. Nandi, S.,[#] Ghosh, S.,[#] **Garg, S.** and Ghosh, S., **2024**. Unveiling the Human Brain on a Chip: An Odyssey to Reconstitute Neuronal Ensembles and Explore Plausible Applications in Neuroscience. *ACS Chem. Neurosci., 15(21), pp.3828-3847*

.

5. Samat, R., Sen, S., Jash, M., Ghosh, S., **Garg, S.,** Sarkar, J. and Ghosh, S., **2024**. Venom: A Promising Avenue for Antimicrobial Therapeutics. *ACS Infect. Di*s., *10(9), pp.3098-3125.*

6. Garg, S, Jana, A., Khan, J., Gupta, S, Roy, R., Gupta, V., and Ghosh, S., **2024**. "Logic "AND Gate Circuit" Based Mussel Inspired Polydopamine Nanocomposite as Bioactive Antioxidant for Management of Oxidative Stress and Neurogenesis in Traumatic Brain Injury". *ACS Appl. Mater. Interfaces., 16, 28, 36168-36193*

7. Gharai, P.K., Khan, J., Pradhan, K., Mallesh, R., **Garg, S.,** Arshi, M.U., Barman, S. and Ghosh, S., **2024**. Power of Dopamine: Multifunctional Compound Assisted Conversion of the Most Risk Factor into Therapeutics of Alzheimer's Disease. *ACS Chem. Neurosci., 15(13), pp.2470-2483*

8. Mallesh, R., Khan, J., Gharai, P.K., Arshi, M.U., **Garg, S.,** Gupta, S. and Ghosh, S., **2024**. Hydrophobic C-Terminal Peptide Analog Aβ31–41 Protects the Neurons from Aβ-Induced Toxicity. *ACS Chem. Neurosci.,* 15(12), pp.2372-2385

9. Gupta, V., Gharai, P.K., Kar, C., **Garg, S.** and Ghosh, S., **2024**. Ratiometric Fluorescent Probe Promotes Trans-differentiation of Human Mesenchymal Stem Cells to Neurons. *ACS Chem. Neurosci.*, *15*(2), pp.222-229.

10. Bhosle, A.A., Banerjee, M., Saha, S., **Garg, S.,** Ghosh, S. and Chatterjee, A., **2023**. An NIR-emissive AIEgen with dual sensing ability: An azine-based chemodosimeter for discriminative ppb-level detection of hydrazine and bisulfite ions. *Sens Actuators B Chem*., *397*, p.134661.

11. Mallesh, R., Khan, J., Gharai, P.K., Ghosh, S., **Garg, S.,** Arshi, M.U. and Ghosh, S., **2023**. High-Affinity Fluorescent Probes for the Detection of Soluble and Insoluble Aβ Deposits in Alzheimer's Disease. *ACS Chem. Neurosci*., *14*(8), pp.1459-1473.

12. Gharai, P.K., Khan, J., Mallesh, R., **Garg, S.,** Saha, A., Ghosh, S. and Ghosh, S., **2023**. Vanillin benzothiazole derivative reduces cellular reactive oxygen species and detects amyloid fibrillar aggregates in Alzheimer's disease brain. *ACS Chem. Neurosci.*, *14*(4), pp.773-786.

13. Gupta, V., Mahata, T., Roy, R., Gharai, P.K., Jana, A., **Garg, S**. and Ghosh, S., **2022**. Discovery of imidazole-based GSK-3 β inhibitors for transdifferentiation of human mesenchymal stem cells to neurons: A potential single-molecule neurotherapeutic foresight. *Front. mol. neurosci., 15*, p.1002419.

14. Ghosh, S., **Garg, S.** and Ghosh, S., **2020**. Cell-derived exosome therapy: a novel approach to treat post-traumatic brain injury mediated neural injury. *ACS Chem. Neurosci.*, *11*(14), pp.2045-2047.

15. Mukherjee, N., Nandi, S., **Garg, S.,** Ghosh, S., Ghosh, S., Samat, R. and Ghosh, S., **2020**. Targeting chondroitin sulfate proteoglycans: an emerging therapeutic strategy to treat CNS injury. *ACS Chem. Neurosci.*, *11*(3), pp.231-232.

16. Das, G., Ghosh, S., **Garg, S.,** Ghosh, S., Jana, A., Samat, R., Mukherjee, N., Roy, R. and Ghosh, S., **2020**. An overview of key potential therapeutic strategies for combat in the COVID-19 battle. *RSC Adv.*, *10*(47), pp.28243-28266.

17. Mukherjee, N., Nandi, S., Ghosh, S., **Garg, S.** and Ghosh, S., **2019**. Three-dimensional microfluidic platform with neural organoids: model system for unraveling synapses. *ACS Chem. Neurosci.*, *11*(2), pp.101-102.

# Equal Contribution

Patents:

1. Bioactive Antioxidant neuroprotective nanoparticles for combacting ros levels and neuron regeneration in Traumatic Brain injury Ghosh, Surajit, **Garg Shubham**, Jana Aniket, Gupta Sanju, Arshi Umar, Roy Rajsekhar Indian Pat. Appl. (2023), IN 202311054293.

Book Chapters:

1. Facile Method of Tubulin Purification from Goat Brain for Reconstitution of Microtubule-Associated Intracellular Function Satyajit Ghosh, **Shubham Garg**, Nabanita Mukherjee, and Surajit Ghosh*. Microtubules. Methods in Molecular Biology, vol 2430.

2. Brain on a-Chip Subhadra Nandi, Satyajit Ghosh, **Shubham Garg**, Ankan Sarkar and Surajit Ghosh. Microfluidics and Multi Organs on Chip pp 475–493.

3. Organ on a Chip for Multianalyte Monitoring **Shubham Garg**, Arijit Bera, Rajsekhar Roy, Satyajit Ghosh and Surajit Ghosh. Elsevier

Conferences Attended:

1. Attended "**2024 GRS and GRC: The Barriers of the CNS**" held from 8th - 14th June 2024 in New Hampshire, United States. (SERB ITS and Institute Funded)

2. Attended "**Hands-On International Workshop on Microfluidics**" (IMW 2020) held from 24th-28th February 2020 at Shiv Nadar University, Noida, India

Contents

		page
Certificate		*ii*
Declaration		*iii*
Acknowledgements		*Iv*
Abstract		*vi*
List of Publications		*viii*
Contents		*xi*
List of Figures		*xv*
List of Tables		*xxvii*
List of Symbols		*xxvii*
List of Abbreviations		*xxvii*

Chapter 1: Introduction

1.1	*Effective Design Of Nanomaterials For Mitochondria-Targeted Nanotherapeutics*	*1*
1.2	*Structure, Function and Associated Disorder Related to Mitochondria*	*3*
1.3	*Discovery of Mitochondriotrophic*	*5*
	1.3.1 Mitochondria Targeting Small Molecules	*5*
	1.3.2 Mitochondria Targeting Peptides	*6*
	1.3.3 Mitochondria Targeting Polymeric Nanocarriers	*6*
	1.3.4 Mitochondria Targeting Vesicles	*7*
1.4	*Mitochondria-Related Dysfunction Disorders*	*8*
1.5	*Neurological Specific Disorder*	*8*
1.5	*The Future of Mitochondrial Nanomedicine*	*10*
1.6	*References*	*10*

Chapter 2: Mussel-Inspired Polydopamine Nanocomposite as Bioactive Antioxidant for the Management of Oxidative Stress and Neurogenesis in Traumatic Brain Injury

2.1	*ABSTRACT*	*13*
2.2	*INTRODUCTION*	*13*
2.3	*MATERIALS METHODS AND EXPERIMENTAL SECTION*	*17*
	2.3.1 Materials and Reagents	*17*
	2.3.2 Synthesis of MSNs	*17*
	2.3.3 Drug Loading and Synthesis of Amine-Modified MSN	*18*
	2.3.4 Synthesis of PDA-Coated MSNs	*18*
	2.3.5 Characterization of MSNs	*19*
	2.3.6 Determination of Cytotoxicity	*19*
	2.3.7 In Vitro Drug Release	*19*
	2.3.8 DPPH Scavenging Test	*19*
	2.3.9 ABTS Free Radical Scavenging Test	*20*
	2.3.10 In Vitro CCA Assay	*20*
	2.3.11 Assay of Catalase-like Activity	*20*
	2.3.12 Calcein-AM / PI Live Dead Assay for SHSY-5Y Cells	*20*
	2.3.13 Calcein-AM / PI Live Dead Assay of hMSCs with PDA-AMSN	*21*
	2.3.14 Hoechst Staining for Apoptosis	*21*
	2.3.15 Determination of Intracellular Basal ROS Level	*21*
	2.3.16 Measurement of Cellular Oxidative Stress in Live Cells	*22*
	2.3.17 Assessment of CAT Mimetic Study	*22*
	2.3.18 Measurement of Mitochondrial Superoxide ROS	*22*
	2.3.19 Measurement of Mitochondria Membrane Potential	*22*

2.3.20 Western Blotting 22
2.3.21 In Vitro Release of FITC-AMSN from PANAP Hydrogel 23
2.3.22 Cell Culture and Immunocytochemistry of hMSCs 23
2.3.23 Electrophysiology of hMSCs derived Neurons 23
2.3.24 Primary Mixed Culture of Rat Hippocampal Neuron 24
2.3.25 Animals and Experimental Design for Cryogenic Brain Injury 24
2.3.26 Measurement of Brain Edema 24
2.3.27 Determination of Blood-Brain Barrier(BBB) Integrity 25
2.3.28 Tissue Processing and Histochemistry 25
2.3.29 Immunofluorescence 25
2.3.30 Measurement of Proinflammatory Cytokines using ELISA for TNF- and IL-6 25
2.3.31 Manual Analysis of Astrocytes and Microglia Morphology 26
2.3.32 Neurological Functional Assessment 26
2.3.33 Statistical Analysis 26
2.4 RESULTS AND DISCUSSION 26
2.4.1 Synthesis and Characterization of Bioactive Nanoparticles 26
2.4.2 Free Radical Scavenging Ability of Bioactive Nanoparticles 31
2.4.3 Protective Effect of Nanoparticles on Cell-Based Model of Oxidative Stress Injury 34
2.4.4 Effect of Nanoparticles on Mitochondria Morphology and ROS in H_2O_2 Induced Oxidative Stress 37
2.4.5 PDA-AMSNs Protect Neuroblastoma SHSY-5Y Cells against H_2O_2 Induced Apoptosis and Inflammation 41
2.4.6 CAT Mimetic Activity of PDA-AMSN 43
2.4.7 Treatment of hMSCs with PDA-AMSN-D Promotes its Neuronal Differentiation 43
2.4.8 Effect of PDA-AMSN-D on Cortical Neuron and Neurosphere Development from Mixed Primary Neuron Culture 46
2.4.9 Synthesis, Characterization and Measurement of Injectability Property of PANAP Hydrogel 49
2.4.10 PDA-AMSN-D Mitigates the Pathological Lesion on Brain Tissue in Cryogenic Brain Injury (CBI) 52
2.4.11 Effect of PDA-AMSN-D on BBB Permeability and Brain Edema after Brain Injury 58
2.4.12 Treatment with PDA-AMSN-D System Effectively Reduced Neuroinflammation and Neuronal Death after CBI 60
2.4.13 PDA-AMSN-D NPs Facilitates the Recovery of Neurological Function Following TBI 67
2.5 CONCLUSION 69
2.6 REFERENCES 69

Chapter 3: Discovery of Mitochondriotropic Antioxidant based on Gallic Acid Attenuates LPS Induced Neuroinflammation via TLR-4, Nrf-2 / Keap-1 Signaling Pathway: Proof of Concept on Cellular and In Vivo Oxidative Stress Model

3.1 ABSTRACT 74
3.2 INTRODUCTION 74
3.3 MATERIALS AND METHODS 77
3.3.1 Materials and Reagents 77
3.3.2 General Procedure of Synthesis 77
3.3.2.1 General Procedure for the Preparation of 1 78
3.3.2.2 General Procedure for the Preparation of 1 78
3.3.2.3 General Procedure for the Preparation of 3a-c 78
3.3.2.4 Characterization of 3a 78
3.3.2.5 Characterization of 3b 79
3.3.2.6 Characterization of 3c 79
3.3.3 Determination of Cytotoxicity 79
3.3.4 DPPH Free Radical Scavenging Test 79

3.3.5 ABTS Free Radical Scavenging Test 79
3.3.6 In Vitro CCA Assay 80
3.3.7 Calcein-AM / PI Live Dead Assay 80
3.3.8 Determination of Intracellular ROS Level 80
3.3.9 Measurement of Cellular Oxidative Stress in Live Cells 81
3.3.10 Measurement of Mitochondrial Superoxide ROS 81
3.3.11 Measurement of Mitochondrial Membrane Potential (ΔΨM) 81
3.3.12 Determination of Cellular Morphology by F-actin Staining 82
3.3.13 RNA Extraction and Quantitative Reverse Transcriptase PCR (RT-qPCR) 82
3.3.14 Immunocytochemistry (ICC) of NFκB Nuclear Translocation 82
3.3.15 Primary Neuronal Culture 82
3.3.16 Animals 82
3.3.17 Serum Stability of Mito-TBA 83
3.3.18 BBB Crossing 83
3.3.19 LPS-Induced Neuroinflammation Model Generation and Drug Administration 83
3.3.20 Open Field Test 84
3.3.21 Sucrose Preference Test 84
3.3.22 Elevated Plus Maze Test 84
3.3.23 Forced Swimming Test 84
3.3.24 Rotarod Test 85
3.3.25 Novel Object Recognition Test 85
3.3.26 Pole Test 85
3.3.27 Morris Water Maze Test 85
3.3.28 Marble Burying Test 86
3.3.29 ELISA 86
3.3.30 Tissue Processing and Histology 86
3.3.31 Immunofluorescence 86
3.3.32 Statistical Significance 87
3.3.33 Figures 87
3.4 RESULTS AND DISCUSSION 87
3.4.1 Design Strategy, Synthesis and Characterization of Mito-TBA 87
3.4.2 Free Radical Scavenging Ability of Mito-TBAs 89
3.4.3 Protective Effect of Mito-TBA-3 on LPS Induced Oxidative Stress Injury in Differentiated PC12 (dPC12) cells 91
3.4.4 Mito-TBA's Rescues dPC12 Cells from LPS Induced Cytotoxicity 93
3.4.5 Mito-TBA's Mitigates Oxidative Stress due to $A\beta_{42}$ and Inhibits Cellular ROS Production in SHSY-5Y Neuroblastoma Cells 97
3.4.6 Impact of Mito-TBA-3 on Mitochondria Morphofunction Impairment and ROS in LPS-induced Oxidative Stress Injury 101
3.4.7 Mito-TBA-3 Inhibits the LPS-Induced Auto-Mitophagy and Restores Mitochondria Network Dynamics 104
3.4.8 Inhibition of Apoptosis and Inflammation by Mito-TBA-3 105
3.4.9 Mito-TBA-3 Inhibits the LPS-Induced Mitochondrial Membrane Potential Disruption and Hyperpolarization in dPC12 Cells 107
3.4.10 Effect of Mito-TBA-3 on F-actin levels in LPS-stimulated dPC12 cells 108
3.4.11 Molecular Docking Analysis 109
3.4.12 Inhibition of LPS-Induced Neuronal Loss and TLR-4 Pathway Mediated Inflammation by Mito-TBA-3 110
3.4.13 Mito-TBA-3 Suppresses LPS-Induced Stress via NFκB Signaling Pathway 113
3.4.14 Mito-TBA-3 attenuates Oxidative Stress Injury by activating Keap1-Nrf-2/ARE Pathway during Selective Autophagy 113
3.4.15 Anti-Apoptotic and Anti-inflammatory Analysis 117

	3.4.16 Neuroprotective Effect of Mito-TBA-3 on $A\beta_{42}$ Induced Toxicity Primary Neuronal Culture	*118*
	3.4.17 In Vivo Validation of LPS-Induced Neuroinflammation Rat Model	*119*
	3.4.18 Assessment of Serum Stability of Mito-TBA-3	*120*
	3.4.19 Assessment of BBB Crossing Efficacy of Mito-TBA-3	*121*
	3.4.20 Mito-TBA-3 Improved Depression and Anxiety like Behaviors in LPS-Induced Neuroinflammation Rat Model	*122*
	3.4.21 Mito-TBA-3 Effectively Mitigates the Locomotive Balance and Motor Impairment in LPS-Induced Neuroinflammation	*124*
	3.4.22 Effective amelioration of Cognitive Impairment in LPS Induced Model Rats by Mito-TBA-3	*128*
	3.4.23 Mito-TBA-3 Restores the Sensorimotor Co-ordination Deficits	*129*
	3.4.24 Mitigation of Compulsive and Repetitive Behavior by Mito-TBA-3	*131*
	3.4.25 Mito-TBA-3 Improves the Depression like Behavior	*132*
	3.4.26 Inhibition of Proinflammatory Cytokines by Mito-TBA-3	*133*
	3.4.27 Treatment with Mito-TBA-3 Effectively Reduces Neuroinflammation & Neuronal Death following Neuroinflammation	*134*
	3.4.28 Mito-TBA-3 Treatment Effectively Reduces Inflammation and Neuronal Death Following LPS Administration	*136*
	3.4.29 Analysis of in vivo Toxicity of Mito-TBA-3 on Different Body Organs	*140*
3.5	*CONCLUSION*	*141*
3.6	*REFERENCES*	*142*

Chapter 4: Brush-Induced Macroscopic Alignment of Self-Assembling Peptide Nanofibers: Potential Therapeutic Lead for Regeneration in Sciatic Nerve Injury

4.1	*ABSTRACT*	*146*
4.2	*INTRODUCTION*	*147*
4.3	*MATERIALS AND METHODS*	*150*
	4.3.1 Multidomain Nanofiber Peptide Synthesis	*150*
	4.3.2 Peptide Hydrogel Preparation for in vitro and in vivo Assays	*150*
	4.3.3 Characterization of Peptide Hydrogel	*151*
	4.3.4 Rheology Study of Peptide Hydrogel	*151*
	4.3.5 Determination of Cytotoxicity of Different Peptide Hydrogels	*151*
	4.3.6 Hydrogel Coated Surface Preparation	*151*
	4.3.7 In Vitro Cytotoxicity Analysis.	*152*
	4.3.8 Scratch Wound Healing Assay with Different Peptide Hydrogels	*152*
	4.3.9 Brush-Induced Orientation and Transdifferentiation of hMSCs	*152*
	4.3.10 Primary Cortical Neuronal Culture	*153*
	4.3.11 Injectability Nature of the Peptide Hydrogel	*153*
	4.3.12 Animals	*153*
	4.3.13 Generation of Sciatic Nerve Crush Injury Model	*153*
	4.3.14 Beam Walking Motor Coordination Assay	*154*
	4.3.15 Calculation of Sciatic Nerve Function Index (SFI)	*154*
	4.3.16 Histology and Staining	*154*
	4.3.17 Haematoxylin and Eosin of Gastromeniscus Muscles	*154*
	4.3.17 Statistical Analysis	*155*
4.4	*RESULTS AND DISCUSSION*	*155*
	4.4.1 Biomimetic SAMDPs spontaneously form nanofibrous scaffolds through self-assembly	*155*
	4.4.2 A Peptide Hydrogel That Assembles Itself and Its Mechanical and Physical Properties.	*156*
	4.4.3 Biocompatibility of the Peptide Hydrogel	*158*
	4.4.4 Investigation of Alignment Parameters	*159*

4.4.5 Scratch Wound Healing Assay 162
4.4.6 hMSCs Align and Differentiate on the Peptide Nanofibers 162
4.4.7 Biomimetic MDPs Promote Neurite Outgrowth In Vitro 168
4.4.8 Histological Analysis of Nerve Regeneration 170
4.4.9 Peptide Hydrogel Attenuated Gastrocnemius Muscle Atrophy in Peripheral Nerve Injury Rats 171
4.4.10 Behavioral Assessment 172
4.4.11 Functional Evaluation of Nerve Regeneration 173
4.4.12 In Vivo Cytotoxicity Analysis 175
4.5 CONCLUSION 176
4.6 REFERENCES 176

Chapter 5: Conclusion and Future Perspective
5.1 Summary 179
5.2 Future Perspective 181
APPENDIX A 182

List of Figures

Figures	Chapter 1	Page
1.1	Intelligent design of nanotherapeutics: Mitochondria are crucial in modulating cellular survival and apoptosis. They have emerged as significant targets in organelle-targeted treatment. This Illustration emphasises a compilation of recent advancements in the design techniques of multifunctional mitochondria-targeted nanotherapeutics	2
1.2	Illustration depicts the complicated architecture of the mitochondrion, emphasising key components such as membrane potential, cardiolipin, translocase complexes (TOM/TIM), and receptor affinities vital for targeted mediated therapy. It underscores the potential for sophisticated treatment approaches via targeted mitochondrial intervention	4
1.3	Mitochondrial dysfunctions in various neurodegenerative illnesses and the specific cell types affected by these dysfunctions	9

Figures	Chapter 2	Page
2.1	Schematic illustration of the PDA-AMSN-D in brain injury	14
2.2	FE-SEM images of the synthesized (A) S-MSN, (B) L-MSN, (C), (D), (E) and (F) size distribution analysis of S-MSN, L-MSN, AMSN & PDA-AMSN, (G) TEM micrograph images of PDA-AMSN, (H) TEM image of single PDA-AMSN, (I) Zeta potential of MSN, AMSN and PDA-AMSN.	27
2.3	Synthetic scheme of imidazole-based neurogenesis molecule (NCM)	28
2.4	(A) 1H & (B) 13C NMR spectra of imidazole-based neurogenesis molecule (NCM) (C) LCMS & (D) HPLC chromatogram of NCM of imidazole-based GSK-3 beta inhibitor neurogenesis molecule.	29
2.5	Characterization of nanoparticles. (A) and (B) Pore size distribution and nitrogen absorption–desorption isotherms of L-MSN and S-MSN, respectively. (C) Drug encapsulation efficiency (EE) and drug loading capacity (DLC) of model drug. (D) and (E) Representative FE-SEM images of AMSN and PDA-AMSN, respectively. Scale bar corresponds to 100 nm. (F) FT-IR spectra of L-MSN, AMSN, and PDA-AMSN. (G) TGA analysis of L-MSN, AMSN, AMSN-D, and PDA-AMSN-D. (H) In vitro drug release profile of AMSN-D at pH 5.5 and 7.4 at different times (n = 3 per group). (I) In vitro drug release profile of PDA-AMSN-D at pH 5.5 and 7.4 at different times (n = 3 per group).	30
2.6	(A) Visual representation of colorimetric change in the DPPH solution upon incubation/addition of or with increasing concentration of PDA-AMSN from left to right. (B) Visual representation of colorimetric change in the ABTS free radical upon reacting with decreasing concentration of PDA-AMSN from left to right. (C) DPPH and ABTS free radical scavenging activity of NCM, (D) In vitro drug release profile of AMSN-D and PDA-AMSN-D at pH 6.8 at different time (n=3 per group). Data represent mean ± SD of three independent experiments	31
2.7	In vitro free radical scavenging activity of PDA-AMSN. (A) DPPH absorbance after treating with different concentrations of PDA-AMSN. (B) DPPH • radical scavenging rate plotted as their percentage of scavenging rate (%) of PDA-AMSN at different concentrations, respectively. (C) ABTS+• absorbance after treating with different concentrations of PDA-AMSN. (D) ABTS+• radical scavenging rate plotted as their percentage of scavenging rate (%) of PDA-AMSN at different concentrations, respectively. (E) Representative illustration of DPPH and ABTS+• scavenging activity of PDA-AMSN. (F) and (G) Normalized and Mean fluorescence intensity (452 nm) of 7-OH-CCA generated in ascorbate assay with different treatment conditions after 1 h incubation at 37 °C. (H) Diagrammatic illustration of the action of PDA-AMSN as a CAT	32

mimetic using TA (terephthalic acid). (I) Fluorescence spectra of TA at various concentrations of PDA-AMSN.

2.8 *Cell viability assay (MTT assay) of SH-SY5Y treated with (A) different concentrations (7-1000 µg/mL) of PDA-AMSN nanoparticles and (B) different wt% of PANAP hydrogel.* 34

2.9 *(A) Cell viability assay (MTT assay) of SH-SY5Y cells upon treating with different concentration of H_2O_2 to determine the inhibitory concentration of H_2O_2. (B) Cell viability of SH-SY5Y cells with pretreated H_2O_2 followed by treatment of different concentration of PDA-AMSN. (C) Cell viability of SH-SY5Y cells with pretreated H_2O_2 followed by treatment of different concentration of PANAP.* 35

2.10 *Protective effect of PDA-AMSN and determination of total cellular ROS against H_2O_2-induced ROS stress in SH-SY5Y cells. Fluorescent microscope images of Hoechst staining of SH-SY5Y cells after different treatment conditions. Scale bar corresponds to 20 µm.* 36

2.11 *Protective effect of PDA-AMSN and determination of total cellular ROS against H_2O_2-induced ROS stress in SH-SY5Y cells. (A) Calcein-AM/PI images of SH-SY5Y treated with H_2O_2 alone, H_2O_2 + AMSN, and H_2O_2 + PDA-AMSN (40 µg/mL). Scale bar corresponds to 200 µm.* 36

2.12 *Fluorescent and DIC Images of DCFH-DA assay for the detection of total ROS level in SH-SY5Y cells.* 37

2.13 *Protective effect of PDA-AMSN and determination of total cellular ROS against H_2O_2-induced ROS stress in SH-SY5Y cells. Fluorescent microscopic and DIC images after staining SH-SY5Y cells with CellROX under different treatment conditions.* 38

2.14 *PDA-AMSN restores mitochondria morphology and reduces H_2O_2-induced oxidative stress in SH-SY5Y cells. Fluorescent microscopy images of Mitotracker Green and MitoSOX Red staining in fixed SH-SY5Y cells, counterstained with DAPI. Scale Bar corresponds to 50 µm.* 39

2.15 *PDA-AMSN restores mitochondria morphology and reduces H_2O_2-induced oxidative stress in SH-SY5Y cells. (A) Single cell images of SHSY5Y to detect mitochondria morphology after treating with PDA-AMSN, H_2O_2, H_2O_2 + AMSN, and H_2O_2 + PDA-AMSN. (B) Analysis of different mitochondrial parameters like perimeter, (C) mitochondria per cell count, (D) circularity, and (E) average size under different treatment conditions (n = 3 per group).* 40

2.16 *PDA-AMSN restores mitochondria morphology and reduces H_2O_2-induced oxidative stress in SH-SY5Y cells. (A) Fluorescent images of JC-1-stained SH-SY5Y images under different treatment conditions. (B) Schematic illustration of the mechanism of JC-1 dye to observe mitochondria depolarization where JC-1 dye shows its reversible fluorescence between its healthy (red fluorescent) and apoptotic (green fluorescent) cells. (C) Quantitative analysis of ratio of aggregates and monomer of JC-1 dye.* 41

2.17 *Schematic illustration of the anti-inflammation and ROS scavenging activity of PDA-AMSN. (A) Western blot analysis of different apoptotic and inflammatory markers in SH-SY5Y cells and its (B) densitometry analysis. (C) Quantitative analysis of TNF-α levels in SHSY5Y cells as determined by ELISA under different treatment conditions. (D) Schematic illustration of the anti-inflammatory and ROS scavenging activity of PDA-AMSN (E) Representative bar graph showing CAT activity in SH-SY5Y cells. Data are presented as means ± standard deviations, n = 3 for each group. Scale Bar corresponds to 50 µm.* 42

2.18 *A) Fluorescent microscopic images of hMSCs counter-stained with DAPI treated with FITC tagged MSN to check the cellular uptake efficiency of AMSN. (B) Calcein-AM / PI images of hMSCs after treatment with different concentration of PDA-AMSN. (C) Quantitative analysis of relative cell viability of hMSCs with different concentration of PDA-AMSN calculated with Image J (n=3 per group). Scale bar corresponds to 200 µm.* 44

2.19 *Cytoskeleton evaluation, characterization of the hMSCs derived neurons and neurogenic potential of PDA-AMNS-D. Fluorescent microscopic images of hMSCs stained with Phalloidin to check the cytoskeleton and counterstained with DAPI under* 46

(A) control condition and after treating with different concertation of PDA-AMSN-D (B) 25 µg/mL, (C) 50 µg/mL, (D) 75 µg/mL for 24 h. Scale bar corresponds to 50 µm.
2.20 Immunocytochemical analysis of hMSCs derived neurons stained with TUJ1 and GFAP under control (A) condition after treating with PDA-AMSN-D (B) and R.A. (C). Scale bar corresponds to 50 µm. 47
2.21 (A) and (B) Electrophysiology of transdifferentiated hMSCs showing spikes upon performing voltage clamp and continuous observation period of 3 minutes, uninterrupted instances of spontaneous creation of electrical impulses respectively. 48
2.22 (A-H) ICC of E18 primary cortical neurons stained with TUJ1 and MAP2 and counterstained with DAPI under control conditions and when treated with (I–L) PDA-AMSN-D. Scale bar corresponds to 200 µm. ICC of primary neurosphere to check the neurogenic efficiency of PDA-AMSN-D without (I) any treatment and when treated with (J) PDA-AMSN-D neurosphere were stained with MAP2 and GFAP. Scale bar corresponds to 50 µm. 49
2.23 (A) ESI Mass spectra & (B) HPLC chromatogram of PANAP peptide. 50
2.24 Viscoelastic property of PANAP peptide; (A) Frequency sweep study, (B) Strain sweep study, (C) Thixotropic study (D) CD spectra & (E) IR spectra of PANAP peptide. 50
2.25 Characterization of PANAP hydrogel; (A) AFM of PANAP hydrogel, (B)Vial inversion test to check the formation of hydrogel. Scale bar corresponds to 1 µm. 51
2.26 Illustration of injectable nature of PANAP hydrogel; (A) PANAP Hydrogel in the vial, (B) Sol" inside injection syringe, (C) "Sol" within the vial, (D) Recovery of "gel" nature within a few minutes as shown with inverted vial. 51
2.27 PDA-AMSN-D reduces tissue damage and helps in tissue regeneration. (A–H) Hematoxylin and Eosin and Cresyl Violet staining of cerebral cortex of rat brain sections on day 7 after CBI. (A, B) Densely packed cells in the Control group with clear neuronal structure as shown in inset and marked with black arrow. (C, D) Cytoplasmic vacuolization and uneven distribution of cells in the injured area as shown in the inset and marked with black arrow. (E, F) Decrease in the injured tissue area, when treated with gel as shown in the inset and marked with black arrow. (G, H) Significant increase in tissue regeneration and decrease in the injured area, cell necrosis as compared to the Injury group as shown in the inset and marked with black arrow. Scale bar corresponds to 100 µm. 53
2.28 PDA-AMSN-D reduces tissue damage and helps in tissue regeneration. Cresyl violent-stained sections of rat cerebral cortex on day 7 after CBI under Control (A, B), Injury (C, D), Gel (E, F), and Gel/PDA-AMSN-D system (G, H). Scale bar corresponds to 100 µm. Scale bar in i–iv corresponds to 50 µm. 54
2.29 Quantification of the repaired area after injury in different group calculated using Image J. (B) Quantification of the expression levels of proinflammatory markers TNF-α and IL-6 in rat brain after CBI with different treatment conditions measured using ELISA technique. 55
2.30 Protective effect of PDA-AMSN-D in TBI. (A-C) Representative images of sham rat brain at D3, D5, and D7, respectively. (D-F) Representative images of injured rat brain after saline treatment at D3, D5, and D7, respectively. (G-I) Representative images of injured rat brain that received only Gel as a treatment after injury at D3, D5, and D7, respectively. (J-L) Representative images of injured rat brain that received Gel/PDA-AMSN-D system as a treatment after injury at D3, D5, and D7, respectively. 56
2.31 Protective effect of PDA-AMSN-D in TBI. (A) Schematic illustration showing the coronal brain section before and after the injury. (B) Evaluation of BBB permeability measured using intravenous injection of EB at day 3 post injury. (C) Quantitative analysis EB leakage in each group (D) Quantitative analysis of Brain edema after post injury. 57
2.32 PDA-AMSN-D attenuated oxidative, inflammatory response in CBI and promotes neurological functional recovery. (A) Fluorescent images of GFAP-stained cortex and straitum section of Control, Injury, Gel, and Gel/PDA-AMSN-D system brain 7 days after 59

	CBI. Highly branched, highly reactive astrocytes are marked with white arrow. (B) Schematic illustration of a single skeletonized microglia with annotations points and its FracLac analysis output. (C) For Sholl analysis, circles show overlaid spheres centered around microglia somata. Scale bar corresponds 50 µm.	
2.33	*Quantification of GFAP stained astrocytes complexity using Sholl analysis of GFAP-stained ipsilateral cortex section of (A) Control, (B) Injury, (C) Gel, and (D) Gel/PDA-AMSN-D system brain 7 days after CBI.*	*60*
2.34	*(A) Fluorescent images of Iba1-stained ipsilateral cortex section of Control, Injury, Gel, and Gel/PDA-AMSN-D system brain 7 days after CBI. Highly branched, highly ramified microglia are marked with green arrow, and deramified amoeboid microglia are marked with yellow arrow. (B) Schematic illustration of a single skeletonized microglia with annotations points and its FracLac analysis output. Scale bar corresponds 50 µm.*	*61*
2.35	*Quantification of microglial dendrite ramification complexity using Sholl analysis of Iba1-stained ipsilateral cortex section of (A) Control, (B) Injury, (C) Gel, and (D) Gel/PDA-AMSN-D system brain 7 days after CBI.*	*62*
2.36	*Increased GFAP astrocytes expression in the ipsilateral section of the hippocampus after CBI. (A-C) Representative images of GFAP immunostaining in the Control, (D-F) Representative images of GFAP immunostaining in the Injury, (G-I) Representative images of GFAP immunostaining in the Gel and (J-L) Representative images of GFAP immunostaining in the Gel / PDA-AMSN-D hippocampus region of brain. Counter stained with DAPI. Scale bar corresponds 200 µm.*	*64*
2.37	*PDA-AMSN-D attenuated oxidative, inflammatory response in CBI and promotes neurological functional recovery. (A) Fluorescent images of GFAP-stained straitum section of Control, Injury, Gel, and Gel/PDA-AMSN-D system brain 7 days after CBI. Highly branched, highly reactive astrocytes are marked with white arrow. (B) Fluorescent images of Iba1-stained straitum section of Control, Injury, Gel, and Gel/PDA-AMSN-D system brain 7 days after CBI. Scale bar corresponds 50 µm.*	*65*
2.38	*Fluorescent images of NeuN-stained (A) cortex and (B) straitum section of Control, Injury, Gel, and Gel/PDA-AMSN-D system brain 7 days after CBI. Neurons with injury and retracted neurite length are marked with red arrow. Neurons with injury and retracted neurite length are marked with red arrow. Scale bar corresponds 50 µm.*	*66*
2.39	*(A), (B) and (C) Quantification of astrocytes, microglia & NeuN in the cortex region.*	*67*
2.40	*MWM behavioral set up for the CBI rats (A) A timeline illustration of the CBI from day 0 of animal grouping to day 7. (B) Representative images of track plots of animals during learning and memory phase.*	*68*
2.41	*(A) Searching time of the platform for each day during the last trial for 5 days. (B–E) Distance to the platform, time spent in target quadrant during the learning phase, time spent at the platform, and number of times platform crossing during the probe trial.*	*68*

Figures	***Chapter 3***	***Page***
3.1	*Schematic illustration of the mechanism of action of Mito-TBA-3 in LPS induced neuroinflammation.*	*88*
3.2	*Synthetic route of substituted 1,3,5 triazine; Reagents and conditions: (i) Na_2CO_3, Acetone, from 0°C (2h) to room temperature (8h), (ii) ACN, Reflux, 15h, (iii) Triethylamine, Ethanol, Reflux, 18h, (iv) BBr_3, from −70 °C (10 min) to room temperature (12 h).*	*89*
3.3	*(A) 1H NMR of 3c (Mito-TBA-3), 13C NMR of 3c (Mito-TBA-3), (B) ESI-MS of 3c (Mito-TBA-3). (C) Expected 677.23 and observed 678.23 [M+H] mass, (D) HPLC spectra of 3c (Mito-TBA-3)*	*89*
3.4	*Evaluation of in vitro effectiveness of Mito-TBA's in scavenging free radicals. (A) The reaction mechanism involved in the scavenging of DPPH• and ABTS• radicals using*	*92*

Mito-TBA. (B) Absorbance of DPPH following treatment with Mito-TBA's (C) & (D) The radical scavenging rates of DPPH• and ABTS• were plotted as a percentage of the scavenging rate (%) of Mito-TBA's at different concentrations along with the positive control Gallic acid. (E) Absorbance of ABTS following treatment with Mito-TBA's. (F) and (G) Bar graph illustrating the normalized and mean fluorescence intensity (452 nm) of 7-OH–CCA under various treatment conditions. (G) Normalized & Mean fluorescence intensity (452 nm) of 7-OH–CCA measured in an ascorbate assay under different treatment conditions following a 1-hour incubation at 37°C. (H) Cell viability (MTT assay) of Mito-TBA-3 with dPC12 at different concentrations (1.5-200 μM) after 24 hrs. (I) Cell viability (MTT assay) of dPC12 with LPS at different concentrations of LPS (0.62-50 μg/mL) to determine the dose-responsive concentration after 24 hrs.

3.5 *(A) and (B) Cell viability (MTT assay) of Mito-TBA-1 and Mito-TBA-2 with dPC12 at different concentrations (1.5-200 μM) after 24 hrs. (C), (D) and (E) Cell viability (MTT assay) of dPC12 with LPS (50 μg / mL) and Mito-TBA-1, Mito-TBA-2 and Mito-TBA-3 respectively to determine the neuroprotective effect of Mito-TBA's.* 93

3.6 *Neuroprotective effect of Mito-TBA-3 against LPS-induced oxidative stress in dPC12 rat pheochromocytoma cells. Calcein-AM / PI images of dPC12 cells treated with, Mito-TBA-3 alone, LPS, and LPS + Mito-TBA-3. Scale bar corresponds to 200 μm.* 94

3.7 *Neuroprotective effect of Mito-TBA-3 against LPS-induced oxidative stress in dPC12 rat pheochromocytoma cells. (A) The relative cell viability of dPC12 cells, quantitatively analyzed using Image J software. (B) Bar graph showing the quantitatively analysed levels of DCFH-DA staining in dPC12 cells using a microplate reader. The cells were treated with Mito-TBA-3 individually as well as with LPS pretreated dPC12 cells treated with Mito-TBA-3. (C) DIC and Fluorescent Images of DCFH-DA assay were used to determine the overall level of ROS in PC12 cells after Mito-TBA-3 treatment. Scale bar corresponds 200 μm..* 96

3.8 *Neuroprotective effect of Mito-TBA-3 against LPS-induced oxidative stress in dPC12 rat pheochromocytoma cells. DIC and Fluorescent microscopic images of dPC12 cells stained with CellROX under different treatment conditions. Scale bar corresponds to 50 μm.* 97

3.9 *(A), (B) and (C) Cell viability (MTT assay) of Mito-TBA-1, Mito-TBA-2 and Mito-TBA-3 with SH-SY5Y at different concentrations (1.5-200 μM) after 24 hrs. (D), (E) and (F) Cell viability (MTT assay) of SH-SY5Y cells with Aβ42 (10 μM) and Mito-TBA-1, Mito-TBA-2 and Mito-TBA-3 (0.018-10 μM) respectively to determine the neuroprotective effect of Mito-TBA's. (G), (H) and (I) Cell viability (MTT assay) of SH-SY5Y cells with LPS (50 μg / mL) and Mito-TBA-1, Mito-TBA-2 and Mito-TBA-3 (0.018-10 μM) respectively to determine the neuroprotective effect of Mito-TBA's.* 98

3.10 *Neuroprotective effect of Mito-TBA-3 against LPS-induced oxidative stress in dPC12 rat pheochromocytoma cells DIC and Fluorescent Images of DCFH-DA assay used to determine the overall level of ROS in SH-SY5Y cells after Mito-TBA-3 treatment. Scale bar corresponds to 200 μm.* 99

3.11 *Neuroprotective effect of Mito-TBA-3 against LPS-induced oxidative stress in dPC12 rat pheochromocytoma cells. DIC and Fluorescent microscopic images of SH-SY5Y cells stained with CellROX under different treatment conditions. Scale bar corresponds to 50 μm.* 100

3.12 *(A) Representative bar showing quantification of CellROX results to determine the total ROS, obtained from fluorescent microscopy images under different treatment conditions. (B) Calcein-AM / PI images of SH-SY5Y cells pretreated with Aβ42 (10 μM) alone, and Aβ42 (10 μM) + Mito-TBA-3 (C) The relative cell viability of SH-SY5Y cells, quantitatively analyzed using Image J software. Scale bar corresponds to 200 μm.* 101

3.13 *Mito-TBA-3 mitigates mitochondrial oxidative stress, restores mitochondria morphology and alleviates LPS induced oxidative stress in dPC12 cells. Fluorescent microscopy images of Mitotracker-Green (200 nM) and MitoSox-Red (5 μM) staining in* 102

live dPC12 cells, counter stained with DAPI under (A) control, (B) Mito-TBA-3, (C) LPS and (D) LPS + Mito-TBA-3. Scale bar corresponds to 20 µm.

3.14 *Representative fluorescent microscopic image of dPC12 cells stained with the MitoTracker green, Lysotracker red, and Hoechst 33342 under different treated condition (A) control, (B) Mito-TBA-3, (C) LPS and (D) LPS + Mito-TBA-3, (E) Mitochondria dynamic shape, (F) Mitochondria Per cell count, (G) Average Size and (H) Mitochondrial parameters like Perimeter, under different treatment conditions (n=3 per group).* 103

3.15 *Representative fluorescent microscopic image of dPC12 cells stained with the MitoTracker green, Lysotracker red, and Hoechst 33342 under different treated condition (A) control, (B) Mito-TBA-3, (C) LPS and (D) LPS + Mito-TBA-3. Scale bar corresponds to 20 µm* 106

3.16 *Representative fluorescent microscopic image of dPC12 cells stained with Hoechst 33342 to check the nuclear pyknosis under different treated conditions (A) control, (B) Mito-TBA-3, (C) LPS and (D) LPS + Mito-TBA-3. Scale bar corresponds 50µm.* 107

3.17 *Determination of MMP using JC-1 staining, actin filament organization and microtubule structure using Phalloidin staining. Fluorescent microscopic images show JC-1 aggregates (Red, healthy cells) and JC-1 monomers (Green, apoptotic cells) of dPC12 cells stained with JC-1 dye under different treatment conditions control, Mito-TBA-3, LPS and LPS + Mito-TBA-3. Scale Bar corresponds to 50µm.* 108

3.18 *Neuroprotective effect of Mito-TBA-3 against LPS-induced oxidative stress in dPC12 rat pheochromocytoma cells. Analysis of actin fillopodia outgrowth using Phalloidin staining in control, Mito-TBA-3, LPS and LPS + Mito-TBA-3. Scale Bar corresponds to 50µm.* 109

3.19 *(A) Binding site of Mito-TBA-3 with Nrf-2 / Keap1 complex protein (PDB ID: 5NJ8) showing possible binding interactions with key amino acids. (B) Binding model of Mito-TBA-3 with Nrf-2 / Keap1 complex protein (C) Structure of Mito-TBA-3(D) 2D binding interactions of Mito-TBA-3with the important amino acid residues. Purple circles reflects pi-sigma interaction, Pink circles reflects pi-alkyl interaction, yellow circle represent pi-sulfur interaction, light green circle indicates carbon hydrogen bonding, dark green circle indicates covalent hydrogen bonding, sea green circle indicates van der Waals interaction of amino acid residues with ligand.* 110

3.20 *Mito-TBA-3 attenuates pro-inflammatory responses and promotes cytoprotective Effect in dPC12 Cell Lines via Pre-activation of Toll-Like Receptor-4 Signaling Pathway Leading to the Inhibition of Caspase-3/Nuclear Factor-κappa B Pathway. Effect of Mito-TBA-3 on mRNA expression levels of different mediators of TLR-4 / NF-Kb pathway like total (A) TLR 4, (B) MyD88, (C) iNOS, (D) TNFα, (E) IL-6, (F) IL-1β, (G) IL-10, (H) IL-4 with LPS and Mito-TBA-3 treatment using RT-qPCR analysis.* 112

3.21 *Ttranslocation of the NF-κB p65 component of NFκB protein into the nucleus under different treatment conditions (A) control, (B) Mito-TBA-3, (C) LPS and (D) LPS + Mito-TBA-3. Scale bar corresponds 50µm. Scale bar corresponds to 50 µm.* 113

3.22 *Investigating the mechanism by which Mito-TBA-3 mitigates the production of ROS through the Nrf2/ARE signalling pathway and neuroprotective potential of Mito-TBA-3. (A) Effect of Mito-TBA-3 on mRNA expression levels of different antioxidant enzymes like total Nrf2, HO-1, NQO1, GCLC and GCLM in dPC12 cells treated with LPS using qRT-PCR. Immunocytochemical analysis of Nrf-2 expression in the cytoplasm and nucleus under different treatment conditions (B) Control, (C) Mito-TAB-3, (D) LPS and (E) LPS + Mito-TAB-3. Scale bar corresponds to 50 µm.* 116

3.23 *Determination of expression of proinflammatory cytokines and apoptotic markers (A) Western blot analysis of different apoptotic (Bax and Bad) and inflammatory (IL-6) markers in dPC12 cells and its densitometry analysis (B) IL-6, (C) Bax and (D) Bad calculated using Image Lab software of Biorad.* 117

3.24 *ICC of E18 primary cortical neurons stained with TUJ1, MAP2 and counter stained with Hoechst 33342, under (A) control condition and when treated alone with (B) Aβ and (C) Aβ + Mito-TBA-3. Scale bar corresponds to 50 µm.* 118

3.25 *Determination of expression of GFAP with different doses of LPS, (A) Western blot analysis of GFAP in LPS induced rat brain and its (B) densitometry analysis calculated using Image Lab software of Biorad.* 120

3.26 *Estimation of effective dose of Mito-TBA-3, (A) Western blot analysis of GFAP in LPS-induced rat brain after treatment with different doses of Mito-TBA-3, and its (B) densitometry analysis.* 120

3.27 *Estimation of serum stability of Mito-TBA-3, (A) Serum stability of Mito-TBA-3 for 120 h.* 121

3.28 *ESI-MS of rat brain homogenate for Mito-TBA-3, molecular peak at the inset image indicated Mito-TBA-3 crosses the BBB. Expected mass 677.2300 Da, observed mass 677.2311 Da [M] and 675.2154 Da [M-2H].* 122

3.29 *Mito-TBA-3 attenuated depression and anxiety-like behaviour in LPS-induced neuroinflammatory model rats. (A) Schematic depiction of the experimental procedure followed to generate neuroinflammatory model rats: rats were intraperitoneally injected with LPS to induce neuroinflammatory-mediated anxiety and depression-like behaviour, which was successfully alleviated by Mito-TBA-3. The therapeutic effect of Mito-TBA-3 was evaluated by anxiety and depression-like behaviour tests, including sucrose preference test (SPT), Rotarod test, Elevated Plus Maze test (EPM), Open field test (OFT), Novel object recognition test (NORT), Forced Swimming test (FST) and pole test. (B) Schematic illustration of the experimental procedure followed to evaluate anxiety behaviour. Corresponding bar graph with data points showing (C) entries into the open arm and (D) time spent in the open arm. (E) Illustration of rat in the FST paradiagm, (F) Corresponding bar graph showing immobility duration shown by rats in FST.* 123

3.30 *(A) Schematic illustration of the procedure followed to assess locomotor and anxiety-like behaviour in LPS-induced neuroinflammatory model rats. (B) Representative activity tracking plot of the rats under different treatment conditions.* 124

3.31 *Representative activity tracking and the corresponding bar graph showing (A) immobility time, (B) speed, (C) total distance travelled in the OF arena, (D) total lines crossed in the central zone of the OF, (E) total lines crossed in the peripheral zone of the OF, (F) total distance travelled in the central zone, (G) total time spent the central zone, (H) total number of entries made into the central zone.* 125

3.32 *Assessment of motor coordination, locomotor activity and cognitive impairment in LPS induced rats. (A) Schematic illustration of the experimental procedure followed to perform the rotarod test, starting from training on day 0 to the final day of test performance. Rats were trained as described in the Figure, and different parameters were assessed during the test. LPS administration caused a significant loss in motor coordination in rats, as shown by a decrease in (B) Latency to fall from the rod and (C) an increase in a total number of falls. (D) Representative images of the rat performance on rotarod test.* 127

3.33 *(A) Schematic illustration of the experimental procedure followed to assess the cognitive behaviour in LPS-induced rats. (B) Representative tracking plot of the NORT, (C) Bar graph showing exploration time spent by rats with novel and familiar objects, (D) Discrimination index showing the amount of time spent exploring the novel object as compared to the familiar object. (E) Bar graph showing the time to remove the adhesive test from the forelimb.* 128

3.34 *Assessment of motor coordination function by pole test. (A) Bar graph showing total time required to descent in the pole and (B) Bar graph showing time required to take the T-Turn. (C) Bar graph searching time of the platform, (D) Representative track plots of MWM in learning phase of training by different treatment groups, (E) Time spent in the target quadrant, (F) Distance to the platform. Data are represented as the mean ±* 129

s.d. from three independent experiments. Mito-TBA-3 effectively helps in restoring motor coordination as evident from the decrease in time to descent and number of T-turns.

3.35 (A) Schematic illustration of the procedure followed for MBT and SPT, (B, C) Representative images of the MBT under different treatment conditions showing the repetitive compulsive behavior in LPS induced rats. Mito-TBA-3 treatment could inhibit the onset of compulsive like behavior after LPS administration as evident with the decrease in marbles buried in (D) Bar graph showing number of marbles buried, decrease in (E) total time spent in digging and increase in (F) sucrose intake, (G) Representative images of the rats set up in SPT. Data are represented as the mean ± s.d. from three independent experiments. Mito-TBA-3 effectively helps in restoring motor coordination as evident from the decrease in time to descent and number of T-turns. 132

3.36 Neuroprotective effect of Mito-TBA-3 on expression of different proinflammatory cytokines in the Hippocampus and total brain homogenate of LPS induced mice model of learning and memory impairment. (A) Schematic illustration of the procedure followed for the detection of inflammatory cytokines by ELISA assay. Bar graph showing expression level of proinflammatory cytokine (B) TNF-α and (C) IL-6 total brain homogenate in LPS induced rats before and after Mito-TBA-3 and Aspirin treatment. Expression level of proinflammatory cytokine (D) TNF-α and (E) IL-6 total Hippocampus region of the brain in LPS induced rats before and after Mito-TBA-3 and Aspirin treatment. 134

3.37 (A) Representative Hematoxylin and Eosin stained images of the DG, Hippocampus CA1 and CA3 region of the control group rat showing no karyopyknosis; dispersed nucleus shown with the black arrow and no sign of neuropil vacuolization, (B) Representative Hematoxylin and Eosin stained images of the DG, Hippocampus CA1 and CA3 region of the LPS group showing significantly higher number of neurons with necrosis, damage area, cytoplasmic shrinkage and vacuolization as shown with the red diamond (C) Representative Hematoxylin and Eosin stained images of the DG, Hippocampus CA1 and CA3 region of the Mito-TBA-3 treatment group with significantly less tissue damage and necrosis and well distribution of cells as shown with green arrow, (D) Representative Hematoxylin and Eosin stained images of the DG, Hippocampus CA1 and CA3 region of the Aspirin treatment group showing decrease in cell necrosis and shrinkage in cell body as marked with yellow arrow. 135

3.38 (A) Representative cresyl violet stained images of the DG, CA1 and CA3 region of the control group showing healthy neurons with no sign of karyopyknosis, hyperchromasia or neurophil vacoulation as shown with the with arrow, (B) Representative cresyl violet stained images of the DG, CA1 and CA3 region of the LPS group showing significantly high number of neurons with hyperchromasia, pyknosis, karyopyknosis and neurophil vacoulation as shown with the red arrow (C) Representative cresyl violet stained images of the DG, CA1 and CA3 region of the Mito-TBA-3 treatment group with significantly less necrotic nuclei and karyoknosis as shown with green arrow, (D) Representative cresyl violet stained images of the DG, CA1 and CA3 region of the Aspirin treatment group showing less necrotic neuronal nuclei, pyknosis and shrinkage in cell body as marked with yellow arrow. 137

3.39 Mito-TBA-3 attenuated oxidative stress and inflammatory response in LPS induced Neuroinflammation. (A, E) Representative fluorescent microscopic images of the GFAP control group section of cortex and hippocampus region respectively, the astrocytes are not activated and less branched in the control group. (B, F) Representative fluorescent microscopic images of the LPS group section of cortex and hippocampus region respectively, astrocytes are in highly branched state due to the excessive ROS production. (C, G) Representative fluorescent microscopic images of the Mito-TBA-3 treatment group section of cortex and hippocampus region respectively, Mito-TBA-3 138

	could able to reverse the inflammation caused due to LPS administration, as evident with less branched astrocytes and decrease in count of astrocytes. (D, H) Representative fluorescent microscopic images of the Aspirin section of cortex and hippocampus region respectively, as evident Aspirin were able to inhibit the inflammation and the astrocytes returned to their homeostatic morphology. Scale bar corresponds to 50 µm.	
3.40	*Fluorescent images of Iba1 stained cortex and Hippocampus section of Control, LPS, LPS + Mito-TBA-3 and LPS + Aspirin, Mito-TBA-3 was injected 30 minutes after LPS administration at a dose of 0.5 mg/Kg, Amoeboid Shape microglia are marked with the white arrow, healthy microglia with projections are marked with a white star. (A, E) Representative fluorescent microscopic images of the control group section of cortex and hippocampus region respectively, the microglia are in healthy state with ramified morphology and long projections, (B, F) Representative fluorescent microscopic images of the LPS group section of cortex and hippocampus region respectively, the microglia are in amoeboid shape due to high inflammation, (C, G) Representative fluorescent microscopic images of the Mito-TBA-3 treatment group section of cortex and hippocampus region respectively, Mito-TBA-3 could able to reverse the inflammation caused due to LPS administration. (D, H) Representative fluorescent microscopic images of the Aspirin section of cortex and hippocampus region respectively, as evident Aspirin were able to inhibit the inflammation and the microglia are in healthy state with ramified morphology and long projections. Scale bar corresponds to 50 µm.*	*139*
3.41	*(A, E) Representative fluorescent microscopic images of the control group section of cortex and hippocampus region respectively, the neurons are in healthy state with long neurite outgrowth. (B, F) Representative fluorescent microscopic images of the LPS group section of cortex and hippocampus region respectively, the neurons are with degenerative neurite length due to the excessive ROS production. (C, G) Representative fluorescent microscopic images of the Mito-TBA-3 treatment group section of cortex and hippocampus region respectively, Mito-TBA-3 could able to reverse the inflammation caused due to LPS administration, as evident with retrenching of neurons and increase in neuronal cell count. (D, H) Representative fluorescent microscopic images of the Aspirin section of cortex and hippocampus region respectively, as evident Aspirin were able to inhibit the inflammation and the neurons are in healthy state with long dendrites. Scale bar corresponds to 50 µm.*	*140*
3.42	*Representative images of the different organs from the different treatment groups for the evaluation of in vivo cytotoxicity analysis: (A-F) Shows the spleen H & E sections from control, 5 mg/Kg and 10mg/Kg of Mito-TBA-3 at Day 7 (A, C, E) and Day 14 (B, D, F) respectively, (G-L) Shows the lung H & E sections from control, 5 mg/Kg and 10mg/Kg of Mito-TBA-3 at Day 7 (G, I, K) and Day 14 (H, J, L) respectively, (M-R) Shows the liver H & E sections from control, 5 mg/Kg and 10mg/Kg of Mito-TBA-3 at Day 7 (M, O, Q) and Day 14 (N, P, R) respectively, (S-X) Shows the liver H & E sections from control, 5 mg/Kg and 10mg/Kg of Mito-TBA-3 at Day 7 (S, U, W) and Day 14 (T, V, X) respectively. Scale bar corresponds 200 µm.*	*141*

Figures ***Chapter 4*** ***Page***

4.1	*(A) ESI Mass spectra of K2(SL)6K2NAP peptide, (B) ESI Mass spectra of K2(SL)6K2NAV peptide, (C) HPLC of K2(SL)6K2NAP peptide, (D) HPLC of K2(SL)6K2NAV peptide.*	*146*
4.2	*Schematic illustration of the mechanism of action of peptide hydrogel for the treatment of SNI.*	*149*
4.3	*(A) ESI Mass spectra of $K_2(SL)_6K_2$NAP peptide, (B) ESI Mass spectra of $K_2(SL)_6K_2$NAV peptide, (C) HPLC of $K_2(SL)_6K_2$NAP peptide, (D) HPLC of $K_2(SL)_6K_2$NAV peptide*	*155*
4.4	*AFM characterization of the $K_2(SL)_6K_2$ peptide nanofiber, (B) FT-IR spectroscopy of the $K_2(SL)_6K_2$NAP and $K_2(SL)_6K_2$NAV peptide nanofibers confirming generation of b sheets.*	*157*

(C) CD spectra confirming formation of beta sheet structure, (D), (E), (F) Strain sweep study of $K_2(SL)_6K_2$, $K_2(SL)_6K_2$NAP and $K_2(SL)_6K_2$NAV respectively, (G), (H), (I) Dynamic frequency sweep study of $K_2(SL)_6K_2$, $K_2(SL)_6K_2$NAP and $K_2(SL)_6K_2$NAV respectively. Scale bar corresponds to 1μm.

4.5 *AFM images of (A) $K_2(SL)_6K_2$NAP and (B) $K_2(SL)_6K_2$NAP peptide nanofibers. Scale bar corresponds to 1 μm.* 158

4.6 *Cell viability assay (MTT assay) of hMSCs treated with different wt% of (A) $K_2(SL)_6K_2$, (B) $K_2(SL)_6K_2$NAP and (C) $K_2(SL)_6K_2$NAV hydrogel, Cell viability assay (MTT assay) of WI-38 treated with different wt% of (D) $K_2(SL)_6K_2$, (E) $K_2(SL)_6K_2$NAP and (F) $K_2(SL)_6K_2$NAV hydrogel, Cell viability assay (MTT assay) of C2C12 treated with different wt% of (G) $K_2(SL)_6K_2$, (H) $K_2(SL)_6K_2$NAP and (I) $K_2(SL)_6K_2$NAV hydrogel. Data are represented as the mean ± s.d. from three independent experiments. Significances are marked as *P < 0.05, **P < 0.01, and ***P < 0.001; one-way analysis of variance (ANOVA).* 160

4.7 *Cytoskeleton evaluation of hMSCs cultured on different peptide hydrogels. Fluorescent microscopic images of hMSCs stained with Phalloidin to check the cytoskeleton and counterstained with DAPI after treating with different peptides Control (A), $K_2(SL)_6K_2$ (B), $K_2(SL)_6K_2$NAP (C) and $K_2(SL)_6K_2$NAV (D)for 24 h. Cytoskeleton evaluation of C2C12 cultured on different peptide hydrogels. Fluorescent microscopic images of C2C12 stained with Phalloidin to check the cytoskeleton and counterstained with DAPI after treating with different peptides Control (E), $K_2(SL)_6K_2$ (F), $K_2(SL)_6K_2$NAP (G) and $K_2(SL)_6K_2$NAV (H)for 24 h. Scale bar corresponds to 50 μm.* 161

4.8 *Live and Dead assessment of hMSCs. Calcein-AM / PI images of hMSCs under Control (A, E, I), $K_2(SL)_6K_2$ (B, F, J), $K_2(SL)_6K_2$NAP (C, G, K) and $K_2(SL)_6K_2$NAV (D, H, L) treatment with different peptide hydrogel at different point of time Day 3 and under Control (M, Q, U), $K_2(SL)_6K_2$ (N, R, V), $K_2(SL)_6K_2$NAP (O, S, W) and $K_2(SL)_6K_2$NAV (P, T, X) at Day 7. Scale bar corresponds to 200 μm* 162

4.9 *(A), (B) AFM images of $K_2(SL)_6K_2$NAP peptide nanofibers (C) Vector field of aligned cells where the orientation is evaluated for every patch of the image based which allows to visualize the orientation of the vector (D) Orientation calculated from the orientation J, (E) Orientation angle derived from orientation J plugin (F) Coherency map: coherency values close to 1.0 are represented in white, coherency values close to 0.0 are represented in black, (G) The color representation reflects the different orientations, (H), (I) DIC and FITC tagged $K_2(SL)_6K_2$NAP, (J) Coherency map: coherency values close to 1.0 are represented in white, coherency values close to 0.0 are represented in black, (K) The color representation reflects the different orientations (L) Orientation angle derived from orientation J plugin (M) The color representation reflects the different orientations. Scale bar corresponds to 1 μm in (A) and 200 μm in (H) and (I) respectively.* 163

4.10 *(A) SEM of $K_2(SL)_6K_2$NAP peptide nanofibers, (B) Vector field of aligned cells where the orientation is evaluated for every patch of the image based which allows to visualize the orientation of the vector (C) Orientation calculated from the orientation J, (D) Orientation angle derived from orientation J plugin (E) Coherency map: coherency values close to 1.0 are represented in white, coherency values close to 0.0 are represented in black, (F) The color representation reflects the different orientations. (G), (H) DIC and FITC tagged $K_2(SL)_6K_2$NAP, (I) Coherency map: coherency values close to 1.0 are represented in white, coherency values close to 0.0 are represented in black, (J) The color representation reflects the different orientations (K) Orientation angle derived from orientation J plugin (L) The color representation reflects the different orientations. Scale bar corresponds 200 μm in (G) and (H) respectively.* 164

4.11 *Alignment and differentiation of hMSCs derived neurons. (A) Fluorescent images of the hMSCs derived neurons cells with the induction of differentiation for 7 days with $K_2(SL)_6K_2$ conditions. (B) Vector field of aligned cells where the orientation is evaluated for every patch of the image based which allows to visualize the orientation of the vector (C) Coherency map: coherency values close to 1.0 are represented in white,* 165

coherency values close to 0.0 are represented in black (D) Orientation calculated from the orientation J (E) The color representation reflects the different orientations. (F) Fluorescent images of the hMSCs derived neurons cells with the induction of differentiation for 7 days with $K_2(SL)_6K_2$ conditions. (G) Vector field of aligned cells where the orientation is evaluated for every patch of the image based which allows to visualize the orientation of the vector (H) Coherency map: coherency values close to 1.0 are represented in white, coherency values close to 0.0 are represented in black (I) Orientation calculated from the orientation J (J) The color representation reflects the different orientations. (K) Fluorescent images of the hMSCs derived neurons cells with the induction of differentiation for 7 days with $K_2(SL)_6K_2$ conditions. (L) Vector field of aligned cells where the orientation is evaluated for every patch of the image based which allows to visualize the orientation of the vector (M) Coherency map: coherency values close to 1.0 are represented in white, coherency values close to 0.0 are represented in black (N) Orientation calculated from the orientation J (O) The color representation reflects the different orientations. Scale bar corresponds to 200 µm.

4.12 *Cell scratch assay for the evolution of wound closure at various time points (0-24h): (A-D) wound closure on control TCPs without any external factor, (E-H) wound closure on $K_2(SL)_6K_2$ hydrogel treated TCPs, (I-L) wound closure on $K_2(SL)_6K_2$NAP hydrogel treated TCPs, (M-P) wound closure on $K_2(SL)_6K_2$NAV hydrogel treated TCPs. Scale bar corresponds to 200 µm* 166

4.13 *Alignment and differentiation of hMSCs derived neurons. Fluorescent images of the hMSCs derived neurons cells with the induction of differentiation for 7 days with different treatment conditions $K_2(SL)_6K_2$ (A), $K_2(SL)_6K_2$NAP (D) and $K_2(SL)_6K_2$NAV (G). The graphs are corresponding histograms of the angular distribution of neurons with different treatment conditions $K_2(SL)_6K_2$ (B), $K_2(SL)_6K_2$NAP (E) and $K_2(SL)_6K_2$NAV (H). Illustrations of the corresponding vector field of the angular distribution of neurons with different treatment conditions $K_2(SL)_6K_2$ (C), $K_2(SL)_6K_2$NAP (F) and $K_2(SL)_6K_2$NAV (I) Fluorescent images of the hMSCs derived neurons cells at higher magnification of 60x. Cells were stained for anti-Tuj1 (green), anti-actin (red) and DAPI (blue). Scale bars indicate 100 µm in A, D, G and 20 µm in J and K.* 167

4.14 *Differentiation of hMSCs derived neurons on different peptide hydrogel. Fluorescent images of the hMSCs derived neurons cells with the induction of differentiation for 7 days with different treatment conditions Control (A), $K_2(SL)_6K_2$ (B), $K_2(SL)_6K_2$NAP (C) and $K_2(SL)_6K_2$NAV (D).* 168

4.15 *ICC of E18 primary cortical neurons stained with TUJ1, MAP2 and counter stained with Hoechst 33342, under (A) control condition and when treated with $K_2(SL)_6K_2$ (B), $K_2(SL)_6K_2$NAP (C), $K_2(SL)_6K_2$NAV (D). Scale bar corresponds to 50 µm.* 169

4.16 *Generation of neurosphere. Generation of hMSCs derived neurosphere on different peptide hydrogels $K_2(SL)_6K_2$ (A), $K_2(SL)_6K_2$NAP (B) and $K_2(SL)_6K_2$NAV (C) for 7 days. Scale bar corresponds to 200 µm. (D) and (E) SEM image of Generation of neurosphere from primary cortical neuron. Scale bar corresponds to 3 µm in (D) and 500 nm in (E).* 170

4.17 *Structural methodology for assessing nerve tissue regeneration following crush injury. (A-F) Bright-field images of HE-stained transverse sections of sciatic nerves of rats belonging to different groups: control (A), sham-operated (B), $K_2(SL)_6K_2$ (C), $K_2(SL)_6K_2$NAP (D) $K_2(SL)_6K_2$NAV (E) and matrigel (F). Bright-field images of HE-stained cross section of gastrocnemius muscle belonging to different groups: control (G), sham-operated (H), $K_2(SL)_6K_2$ (I), $K_2(SL)_6K_2$NAP (J) $K_2(SL)_6K_2$NAV (K) and matrigel (L). Scale bar corresponds 200 µm.* 171

4.18 *Representative images of (A) Sciatic crush nerve injury model generation with different steps and treatment administration. (B) Representative images of the rat footprint in calculating the SFI (C) Effect of different treatment group on SFI under crush injury and different treatment group. (D) Effect of different treatment group on SFI walking tract* 173

footprints under crush injury and different treatment groups. Data are represented as the mean ± s.d. from three independent experiments.

4.19 *Schematic illustration of the (A) beam walking test to evaluate the functional recovery following nerve regeneration. (B) Representative images of the rat performance in the beam walking test under crush injury, different treatment conditions $K_2(SL)_6K_2$, $K_2(SL)_6K_2$NAP and $K_2(SL)_6K_2$NAV and positive control matrigel. (C) Typical cross time of different treatment groups to cross the group. (D) Foot slip errors per step of the crush injury, different treatment group during the beam walking task, broken down by percentage. Data are represented as the mean ± s.d. from three independent experiments. Significances are marked as *P< 0.05, **P< 0.01, **** P < 0.0001 versus the control group, $^{\#\#}$P<0.05, $^{\#\#}$P<0.01 $^{\#\#\#\#}$ P < 0.0001 versus the crush injury group.* 174

4.20 *Representative images of the different organs harvested from the different peptide hydrogel treatment groups for the evaluation of in vivo cytotoxicity analysis (A-C) Shows the kidney H & E sections from control, $K_2(SL)_6K_2$, $K_2(SL)_6K_2$NAP and $K_2(SL)_6K_2$NAV group at the end of 14 days respectively, (D-F) Shows the liver H & E sections from control, $K_2(SL)_6K_2$, $K_2(SL)_6K_2$NAP and $K_2(SL)_6K_2$NAV group at the end of 14 days respectively (G-I) Shows the spleen H & E sections from control, $K_2(SL)_6K_2$, $K_2(SL)_6K_2$NAP and $K_2(SL)_6K_2$NAV group at the end of 14 days respectively, (J-L) Shows the kidney H & E sections from control, $K_2(SL)_6K_2$, $K_2(SL)_6K_2$NAP and $K_2(SL)_6K_2$NAV group at the end of 14 days respectively. Scale bar corresponds 200 µm.* 175

List of Tables

Table	Title	page
2.1	Tabular representation of AND logic gate responses for total functional recovery	18
3.1	Antioxidant Properties of Mito-TBA-3s and Gallic Acid	91
3.2	Primers Sequence Used for qRT-PCR	112
4.1	Peptide sequence of diiferent SAMDPs	171

List of Symbols

Symbol	Description
Aβ	Amyloid Beta
μ	Micrometer
$^{\circ}C$	Temperature
G'	Storage Modulus
G''	Loss Modulus
L	Length
γ	Shear Strain

List of Abbreviations

Abbreviation	Fullform
Ph.D.	Doctor of Philosophy
TBI	Traumatic Brain Injury
NCM	Neuro Chemical Modulator
MSN	Mesoporous Silica Nanoparticles
PDA	Polydopamine
L-MSN	Large Pore Size Mesoporous Silica Nanoparticles
S-MSN	Pore Size Mesoporous Silica Nanoparticles
AMSN	Amine Modified Mesoporous Silica Nanoparticles
PDA-AMSN	Polydopamine Coated Amine Modified Mesoporous Silica Nanoparticles
PDA-AMSN-D	Polydopamine Coated Amine Modified Mesoporous Silica Nanoparticles loaded with Neuro Chemical Modulator
PANAP	PA-NAPVSIPQKKK Peptide Hydrogel
ROS	Reactive Oxygen Species
BBB	Blood Brain Barrier
ECM	Extracellular matrix
FTIR	Fourier-transform infrared spectroscopy
CD	Circular dichroism

AFM	*Atomic force microscopy*
SEM	*Scanning electron microscopy*
FESEM	*Field emission scanning electron microscopy*
DOPA	*3,4-dihydroxy-1-phenyalanine*
TEM	*Transmission electron microscopy*
MTT	*3-(4,5-dimethylthiazol-2-yl)-2,5-diphenyl Tetrazolium bromide*
CTAB	*Cetyltrimethyammonium Bromide*
DLC	*Drug Loading Capacity*
DEE	*Drug Encapsulation Efficiency*
BET	*Brunauer-Emmett-Teller*
TGA	*Thermogravimetric Analaysis*
DMEM	*Dulbecco's modified Eagle's medium*
DMSO	*Dimethyl sulfoxide*
Fmoc	*Fluorenylmethoxycarbonyl*
CBI	*Cryogenic Brian Injury*
ROS	*Reactive Oxygen Species*
RNS	*Reactive Nitrogen Species*
RP-HPLC	*Reverse Phase-High Pressure Liquid chromatography*
NMR	*Nuclear magnetic resonance*
H_2O_2	*Hydrogen Peroxide*
hMSCs	*Umbilical Cord Derived Mesenchymal Stem Cells*
TA	*Terepthalic Acid*
CCA	*Comurin-3-carboxylic Acid*
MMP	*Mitochondria Membrane Potential*
PBS	*Phosphate buffer saline*
TLR-4	*Toll Like Receptor-4*
Nrf2	*Nuclear Factor Erythroid 2-Related Factor-2*
NDD	*Neurodegenerative Diseases*
dPC12	*Differentiated Pheochromocytoma Cells*
Aβ	*Amyloid Beta*
DCFH-DA	*Dichloro-dihydro-fluorescein Diacetate*
DCM	*Dichloromethane*
DMF	*Dimethyl formamide*
PCR	*Polymerase Chain Reaction*
LPS	*Lipopolysaccharides*
MS	*Mass spectroscopy*
PCR	*Polymerase Chain Reaction*
qRT-PCR	*Real Time PCR*
DPPH	*2,2-diphenyl-1-picrylhydrazyl*
ABTS	*2,2'-azino-bis(3-ethylbenzothiazoline-6-sulfonic acid*
BSA	*Bovine Serum Albumin*
MD	*Molecular dynamics*
PI	*Propidium iodide*
DAPI	*4',6'-diamidino-2-phenylindole*